Journal of Materials Chemistry A

ROYAL SOCIETY OF CHEMISTRY

PAPER

View Article Online
View Journal | View Issue

Check for updates

Cite this: J. Mater. Chem. A, 2025, 13, 12523

Towards robust hydrogen evolution electrocatalysts in immiscible copper–molybdenum alloys by amorphization†

Long Chen,‡[a] Xiying Jian, ‡[a] Qingsheng Gao, [b] Zhijie Cao,[c] Zibo Chen*[d] and Huai-Jun Lin *[a]

Received 24th January 2025
Accepted 25th March 2025

DOI: 10.1039/d5ta00701a

rsc.li/materials-a

Designing bimetallic alloys and providing dual active sites is an effective way to achieve efficient alkaline hydrogen evolution reaction (HER). However, the preparation and determination of an optimal composition remain significant challenges for immiscible alloys. In this study, the amorphous Cu–Mo alloys with a wide composition range were successfully prepared by magnetron sputtering. Among these alloys, the amorphous $Cu_{50}Mo_{50}$ alloy demonstrates excellent alkaline HER activity with low overpotentials of 57 and 149 mV at 10 and 100 mA cm^{-2}, respectively. Moreover, it demonstrates outstanding long-term stability at 300 mA cm^{-2}. The results demonstrate that an electronic interaction exists between the Cu and Mo atoms in the amorphous $Cu_{50}Mo_{50}$ alloy, where the Cu and Mo act as adsorption sites for OH and H intermediates, respectively. Furthermore, the amorphous $Cu_{50}Mo_{50}$ alloy also exhibits favorable intermediates adsorption and water dissociation abilities, which facilitate the alkaline HER process. The research provides a novel insight into the rational design and preparation of advanced alkaline HER catalysts.

1. Introduction

Hydrogen, with its abundant supply, high calorific value and clean combustion, is regarded as a significant means of addressing the energy crisis and environmental pollution problems.[1–3] Electrolysis of water is considered as the most promising strategy for the production of hydrogen, as it can produce high-purity hydrogen and store electrical energy in the chemical bonds of molecular hydrogen.[4–7] Platinum (Pt) has been regarded as an optimal HER catalyst due to its close-to-zero ΔG_{H^*},[8] but the rarity and high cost of Pt metal restrict its extensive application.[9–11] Consequently, it is of paramount significance to develop effective, economical and easily prepared HER catalysts.

Mo-based materials have garnered significant interest as active species for HER.[12–15] However, exploring efficient Mo-based catalysts in HER while achieving long-term stability still faces enormous challenges.[16] Alloying is an efficient method of improving catalyst performance due to the ligand effect caused by the formation of heteroatoms and the strain effect caused by the change in bond length.[17] In a preceding study, the Brewer–Engel valence bond theory was proposed as a guiding principle for the design of advanced HER catalysts.[18] According to the theory, combining the early transition metals with empty or partially filled d-orbitals and the late transition metals with internal paired d-orbitals will result in the remarkable synergistic effect of electrocatalysis.[19] For instance, in the report by Miljanić *et al.*, alloys including Pt_2Mo and Hf_2Fe have been employed as efficient alkaline HER catalysts.[20]

Cu, being a low-cost late transition metal, has attracted considerable interest in recent years, particularly within the field of catalysis.[21] However, the weak hydrogen adsorption properties of Cu have resulted in a paucity of reports on Cu-based catalysts used for HER.[22] In the study by Li and colleagues, the significant role of Cu in the cleaving of H–O bonds in water molecules and the absorption of OH is impressive.[23] In non-acidic conditions, the rate-determining step in HER is usually the sluggish water dissociation process ($H_2O \rightarrow H^* + OH^*$). The high affinity of catalysts for the hydroxyl intermediate (OH*) can facilitate enhanced reaction rates.[24] In light of the aforementioned considerations, alloying Mo with Cu could result in unprecedented alkaline HER performance.

Amorphous materials exhibit long-range disorder structures, which are very different from the crystalline materials.[25] The structural flexibility, adjustable composition and abundance of

[a]Institute of Advanced Wear & Corrosion Resistance and Functional Materials, Jinan University, Guangzhou 510632, PR China. E-mail: hjlin@jnu.edu.cn
[b]Department of Chemistry, Jinan University, Guangzhou, 510632, PR China
[c]College of Physics, Ningxia University, Yinchuan, Ningxia, 750021, PR China
[d]Institute of Chemical & Process Engineering, University of Strathclyde, Glasgow G4 0JQ, UK. E-mail: zibo.chen@strath.ac.uk

† Electronic supplementary information (ESI) available. See DOI: https://doi.org/10.1039/d5ta00701a

‡ Both authors contributed equally to this work.

active sites in amorphous materials render them highly promising as catalysts for HER.[26] Specifically, amorphous catalysts display the following advantages in comparison to their crystalline counterparts: (i) in comparison to crystalline materials with a fixed coordination environment, amorphous materials can be accurately modified at the atomic ratio, which greatly facilitates the design of optimal catalysts with an appropriate elemental ratio; (ii) the increased diffusion of electrolyte into the internal regions of amorphous matrices facilitates the formation of a larger electrolyte–electrocatalyst interface; (iii) amorphous structure is rich in dangling bonds or coordination unsaturated atoms, which may provide more active sites to promote electrochemical processes.[27,28]

The combination of Cu and Mo has been demonstrated in several reports to enhance HER activity.[29,30] However, these reports exclusively consider Cu–Mo alloys with a highly constrained composition range. The activity of an electrocatalyst is significantly affected by its composition.[31] The preparation of amorphous Cu–Mo alloys allow for the effective improvement of the catalytic activity, through the alteration of the composition. It is worthy of note that the Cu–Mo system is immiscible in equilibrium state (Fig. S1†), thus the preparation of Cu–Mo alloys by conventional metallurgy methods remains challenge. The magnetron sputtering technique allows for the direct deposition of a multi-metal catalyst onto a substrate, while simultaneously enabling the alteration of the catalyst's composition and loading.[32] Thus, it is feasible to prepare amorphous Cu–Mo alloys for efficient HER *via* magnetron sputtering.

In this work, we creatively obtained a series of Cu–Mo alloys with a wide composition range in the immiscible Cu–Mo system by magnetron sputtering, and employed them as HER catalysts. Among them, the prepared amorphous $Cu_{50}Mo_{50}$ exhibits optimal HER performance with a low overpotential of 57 mV at 10 mA cm^{-2} and robust long-term stability at 300 mA cm^{-2} in 1.0 M KOH. The final results in this paper prove the feasibility of preparing highly effective alkaline HER catalysts by simple synthesis method and balancing dual active components. This synthesis method and design idea would create more opportunities for developing advanced alkaline HER catalysts.

2. Results and discussion

2.1. Structural characterization

The Cu_xMo_y catalysts were prepared by dual-target magnetron sputtering using porous nickel foam (0.3 mm in height, with an aperture size of 110 PPI) as a substrate. The atomic ratio of the alloys was controllably adjusted by the sputtering power. Similarly, the alloys were deposited on a polymer film for the X-ray diffraction (XRD) analysis, given the strong diffraction peaks exhibited by the nickel foam substrate. The synthesis details and characterization were given in the ESI.†

The phase information of the as-prepared Cu_xMo_y alloys was examined by X-ray diffraction (XRD) analysis, as shown in Fig. 1a. The Cu_xMo_y alloy exhibits an amorphous structure within the atomic ratio range of approximately 43 : 57 to 75 : 25, as evidenced by the presence of weak and broad X-ray diffraction peaks at around 40°. The amorphization of the Cu–Mo alloys rise and then fall, as the Cu content increases. The strong XRD peaks of the Cu film are attributed to Cu (111) and Cu (200) planes (PDF# 04-0836). The strong diffraction peaks observed in the Mo film are attributed to Mo (110) planes (PDF# 42-1120). It can be observed that the diffraction peaks of the crystalline Cu_xMo_y apparently shift to higher angles with increasing Cu content, suggesting lattice contraction caused by the smaller atomic radius of the Cu atom (128 pm) compared to that of Mo (139 pm).[30]

The surface morphology of the $Cu_{50}Mo_{50}$ alloy is shown in Fig. 1b, as obtained by scanning electron microscopy (SEM). The surface of the $Cu_{50}Mo_{50}$ alloy exhibits small island microstructures, a common structure observed during the preparation of alloys by magnetron sputtering.[33] Energy Dispersive X-ray spectroscopy (EDS) elemental mapping images exhibit that Cu and Mo are uniformly distributed on the surface of the $Cu_{50}Mo_{50}$ alloy (Fig. S2†). The results of the cross-sectional EDS images demonstrate that Ni does not diffuse into the $Cu_{50}Mo_{50}$ alloy (Fig. S3†). Fig. 1c presents a transmission electron microscopy (TEM) image of the $Cu_{50}Mo_{50}$ alloy that has been thinned by focused ion beam technology (FIB). We then carried out selected area electron diffraction analysis on the film sample (Fig. 1c and d). The halo ring observed in the selected area electron diffraction pattern (SAED, Fig. 1d) provides further evidence of the formation of amorphous structures in the $Cu_{50}Mo_{50}$ alloy. Fig. 1e together with the inset are high-resolution transmission electron microscopy (HRTEM) image and the corresponding fast Fourier transforms (FFT) image of the $Cu_{50}Mo_{50}$ alloy. The absence of discernible periodic lattice stripes in the HRTEM image and the appearance of diffusion ring in the FFT image illustrate the amorphous structure of the $Cu_{50}Mo_{50}$ alloy.

X-ray photoelectron spectroscopy (XPS) was employed to characterize the valence state information. The XPS survey spectra demonstrate the presence of Cu and Mo elements in the Cu_xMo_y alloys (Fig. 2a). Fig. 2b shows the high-resolution Cu 2p spectra. For the Cu sample, the peaks located at 932.38 and 952.18 eV are correspond to the Cu^0 $2p_{3/2}$ and Cu^0 $2p_{1/2}$, while the signals located at 934.73 and 954.33 eV correspond to the Cu $2p_{3/2}$ and Cu $2p_{1/2}$ of $Cu(OH)_2$ (Cu^{2+}). The signals located at 943.83, 946.65 and 962.37 eV are assigned to the satellite peaks of Cu^{2+}. For the Cu_xMo_y alloys, the peaks located at 932.2–932.6 eV are assigned to Cu $2p_{3/2}$, and the peaks located at 952.1–952.4 eV are assigned to Cu $2p_{1/2}$, which reveal the existence of Cu^+ peaks. The other peaks observed at 943.5–946.8 eV are assigned to the satellite peaks of Cu^+. It is worth noting that all the characteristic peaks of Cu 2p in $Cu_{85}Mo_{15}$ and $Cu_{50}Mo_{50}$ alloys are shifted to lower binding energies compared to $Cu_{28}Mo_{72}$ alloy, indicating an increased electron density of Cu atoms. Fig. 2c displays the Cu LMM spectra to assist in the analysis, as the XPS peak positions of Cu^+ and Cu are indistinguishable. The Cu LMM peak in the range of 918–919 eV is classified as the signal of Cu^0. However, it is difficult to analyze the valence state using the Cu LMM due to the proximity of the peaks of Cu_2O and $Cu(OH)_2$ in the range of 916–917 eV. The presence of $Cu(OH)_2$ peaks in the XPS spectra of Cu 2p (Fig. 2b)

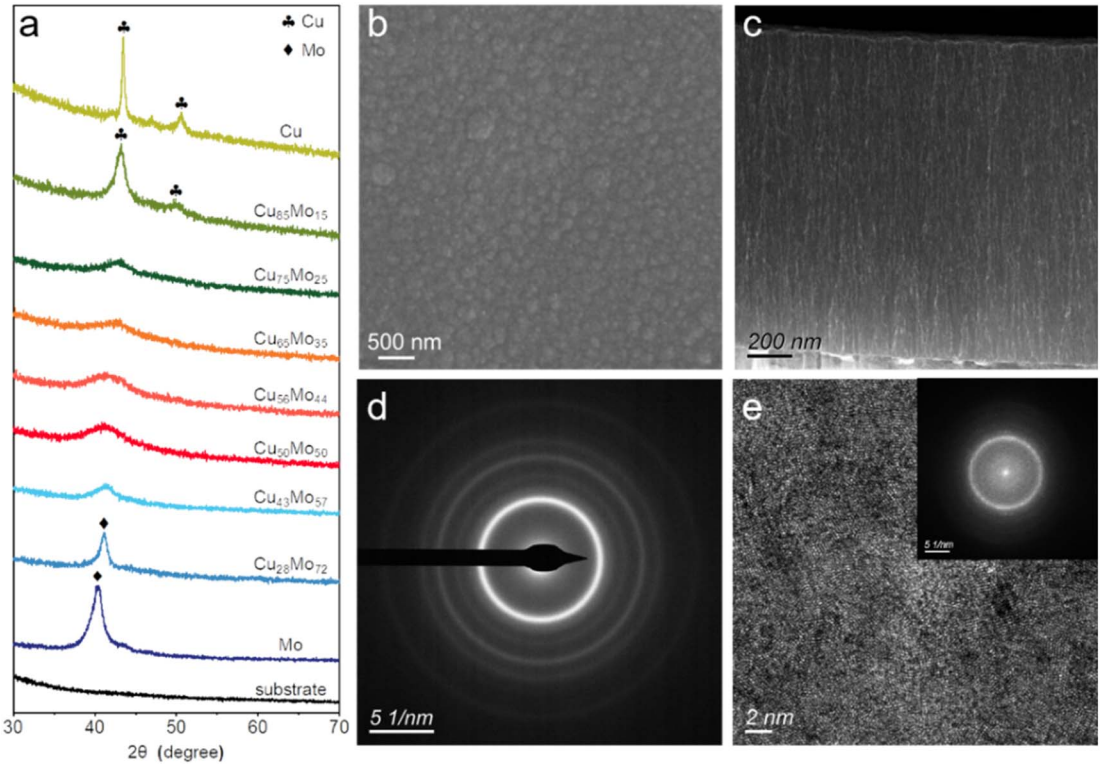

Fig. 1 (a) XRD patterns of the Cu_xMo_y alloys. (b) Surface SEM image. (c and d) Low-magnification TEM image of the $Cu_{50}Mo_{50}$ alloy and the corresponding SAED pattern. (e) HRTEM image of the $Cu_{50}Mo_{50}$ alloy. (Inset) Corresponding FFT pattern.

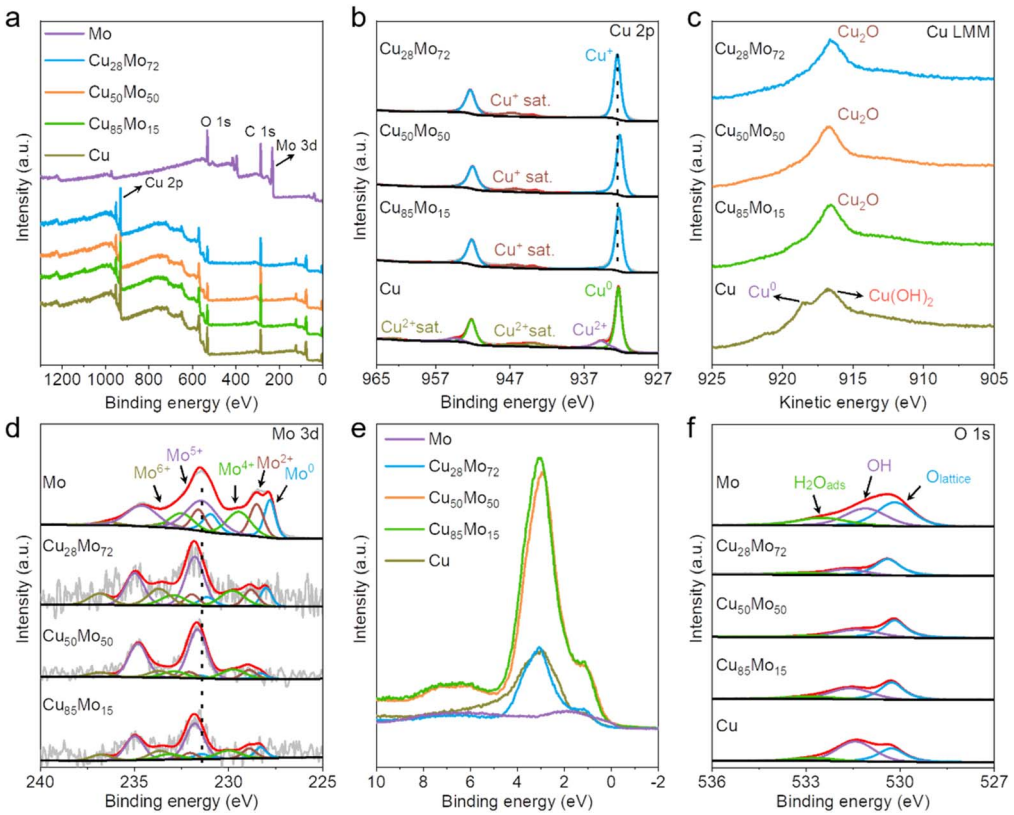

Fig. 2 XPS characterization of the Cu_xMo_y alloys. (a) Survey spectra. (b) Cu 2p. (c) Cu LMM. (d) Mo 3d. (e) Valance band spectra. (f) O 1s.

indicates that the LMM peak in the region of 916–917 eV is $Cu(OH)_2$ for the Cu sample and Cu_2O for the Cu_xMo_y samples (Fig. 2c).

Fig. 2d illustrates that the XPS spectra of Mo 3d shows five spin–orbit doublets. For the Cu_xMo_y alloys, the first doublet at 227.9–228.3 and 231.1–231.5 eV is attributed to Mo^0, while the second doublet at 228.7–228.9 and 231.9–232.1 eV is attributed to Mo^{2+}. The third doublet at 229.7–230.0 and 232.8–232.2 eV corresponds to Mo^{4+}, while the fourth doublet at 231.6–231.8 and 234.8–235.0 eV corresponds to Mo^{5+}. Moreover, the fifth doublet at 233.6–233.7 and 236.7–236.9 eV is assigned to Mo^{6+}. For the Mo sample, the peaks located at 228.0 and 230. 95 eV are assigned to Mo $3d_{5/2}$ and Mo $3d_{3/2}$ of Mo^0, while the peaks located at 228.51 and 231.61 eV correspond to Mo $3d_{5/2}$ and Mo $3d_{3/2}$ of Mo^{2+}. The peaks located at 229.48, 232.53, 231.43 and 234.58 eV are assigned to Mo^{4+} $3d_{5/2}$, Mo^{4+} $3d_{3/2}$, Mo^{5+} $3d_{5/2}$ and Mo^{5+} $3d_{3/2}$, respectively. Additionally, the peaks located at 233.28 and 236.38 eV are attributed to Mo^{6+}. After alloying, the characteristic peaks of Mo 3d in the Cu_xMo_y alloys all shift to higher binding energies than the Mo sample, indicating a decrease in electron density of the Mo atoms (Fig. 2d). This XPS peak shift phenomenon can be attributed to the electron transfer between Cu and Mo. The electronic interaction between Cu and Mo can be further demonstrated by the difference in electronegativity between Cu (1.9) and Mo (1.8).[30] The electronic structure of Cu, $Cu_{85}Mo_{15}$, $Cu_{50}Mo_{50}$, $Cu_{28}Mo_{72}$ and Mo samples is further analyzed by valence band spectra (Fig. 2e). The high density of states (DOS) near the Fermi level exhibited by the $Cu_{85}Mo_{15}$ and $Cu_{50}Mo_{50}$ alloys demonstrates higher carrier concentration, which indicates a modification of the electronic structure. Additionally, the XPS spectra of O 1s were also examined. There are three visible peaks in the O 1s XPS spectra of all samples. For the $Cu_{50}Mo_{50}$ alloy, the three peaks observed at 530.28, 531.43 and 532.80 eV are attributed to metal–oxygen bonds (lattice oxygen), hydroxyl and adsorbed H_2O, respectively (Fig. 2f).

2.2. HER electrocatalytic activity

In order to gain a more comprehensive understanding of the catalytic activity of the crystalline and amorphous Cu_xMo_y alloys, the HER performances of the $Cu_{28}Mo_{72}$ (2.29 mg cm^{-2}), $Cu_{43}Mo_{57}$ (2.01 mg cm^{-2}), $Cu_{50}Mo_{50}$ (2.15 mg cm^{-2}), $Cu_{56}Mo_{44}$ (1.96 mg cm^{-2}) and $Cu_{85}Mo_{15}$ (2.43 mg cm^{-2}) alloys were further investigated. Fig. 3a illustrates that the amorphous $Cu_{43}Mo_{57}$, $Cu_{50}Mo_{50}$ and $Cu_{56}Mo_{44}$ alloys exhibit higher catalytic activity in comparison to the crystalline $Cu_{28}Mo_{72}$ and $Cu_{85}Mo_{15}$. Among these alloys, the amorphous $Cu_{50}Mo_{50}$ exhibits low overpotentials of 57 and 149 mV to achieve 10 and 100 mA cm^{-2} in 1.0 M KOH, respectively. In terms of the catalytic activity of alkaline HER, the Mo sample demonstrates better activity in comparison to Cu, while Ni foam exhibits the lowest activity (Fig. S4†). Fig. 3b provides a comparative illustration of the HER overpotential of Cu_xMo_y in 1.0 M KOH. The amorphous $Cu_{50}Mo_{50}$ catalyst shows a low overpotential at 100 mA cm^{-2} (η_{100}) in 1.0 M KOH, as illustrated in Fig. 3c (the detailed overpotentials at 100 mA cm^{-2} are listed in Table S2†), in comparison to the reported Mo-base or Cu-base HER catalysts. Fig. 3d illustrates that the $Cu_{50}Mo_{50}$ alloy has a small Tafel slope of 85.6 mV dec^{-1}, indicating fast HER kinetics in comparison to other Cu_xMo_y alloys. Tafel plots demonstrate that the Cu–Mo alloys follow the Volmer–Heyrovsky step, with Heyrovsky step acting as the rate determining step (RDS). A large j_0 means that the material has a high intrinsic activity.[34] The values of j_0 for the Cu_xMo_y alloys were obtained by extrapolation from the Tafel plot.[35] The j_0 of the $Cu_{50}Mo_{50}$ alloy is 1.96 mA cm^{-2}, which is larger than those of the $Cu_{28}Mo_{72}$ (1.19 mA cm^{-2}), $Cu_{56}Mo_{44}$ (1.35 mA cm^{-2}) and $Cu_{85}Mo_{15}$ (0.95 mA cm^{-2}) alloys, indicating higher intrinsic activity (Fig. S5†). The charge transfer ability of the catalyst was investigated by means of electrochemical impedance spectroscopy (EIS). Rs represents electrolyte resistance, R_1 is the resistance of microscopic surface roughness, and R_{ct} is the charge transfer resistance.[36] The amorphous $Cu_{43}Mo_{57}$, $Cu_{50}Mo_{50}$ and $Cu_{56}Mo_{44}$ alloys exhibit small charge transfer resistance (R_{ct}), demonstrating a rapid charge transfer process between the electrode surface/electrolyte interface (Fig. 3e).[37] The detailed fitting process of the Nyquist plot of the Cu_xMo_y alloys in 1.0 M KOH is shown in Fig. S6,† and the values of R_{ct} are presented in Table S1.† The electrochemically active area (ECSA) is evaluated by C_{dl} (double-layer capacitance), according to the relation ECSA = C_{dl}/C_s.[33] As illustrated in Fig. 3f and S7,† the C_{dl} value of $Cu_{50}Mo_{50}$ is 45.2 mF cm^{-2}, which is higher than that of the $Cu_{85}Mo_{15}$ alloy (19.3 mF cm^{-2}), indicating that $Cu_{50}Mo_{50}$ expose more active sites. Moreover, with the increase of Cu proportion in the Cu_xMo_y alloys, the C_{dl} in alkaline media gradually decreases. The electrochemical test results demonstrate that amorphous $Cu_{50}Mo_{50}$ alloy exhibits the optimal overall performance for the alkaline HER. To investigate the impact of amorphous structure on catalytic performance, we conducted an annealing experiment on the amorphous $Cu_{50}Mo_{50}$ alloy. After annealing, the amorphous XRD peak observed at around 40° no longer exists, and XRD diffraction peaks corresponding to MoO_2 and CuO appear (Fig. S8a†). The annealed $Cu_{50}Mo_{50}$ requires an overpotential of 237 mV to drive 10 mA cm^{-2}, which is significantly higher than that required for the amorphous $Cu_{50}Mo_{50}$ (Fig. S8b†). The Nyquist plots indicate that the annealed $Cu_{50}Mo_{50}$ exhibits a slower charge transfer rate than that of amorphous $Cu_{50}Mo_{50}$ (Fig. S8c†).

Additionally, the HER performances of the Cu_xMo_y alloys in acidic media were also investigated. Fig. S9a† shows that the Cu_xMo_y alloys with an atomic ratio of 28 : 72 to 56 : 44 exhibit similar LSV curves necessitating an overpotential of approximately 120 and 214 mV to drive 10 and 100 mA cm^{-2}, respectively. Regarding the catalytic activity of acidic HER, it can be observed that the Mo sample exhibits higher activity than Cu, while Ni foam shows the lowest activity (Fig. S10†). As illustrated in Fig. S9b,† the Tafel slope of the $Cu_{50}Mo_{50}$ alloy in an acidic environment is 104.1 mV dec^{-1}, a value that is larger than its 85.6 mV dec^{-1} in an alkaline environment (Fig. 3d). This indicates that the HER process of the $Cu_{50}Mo_{50}$ alloy is slower in the acidic media than in alkaline media. All Cu_xMo_y alloys follow the Volmer–Heyrovsky step in acidic media. As the Cu content in the Cu_xMo_y alloys increases, the Tafel slope

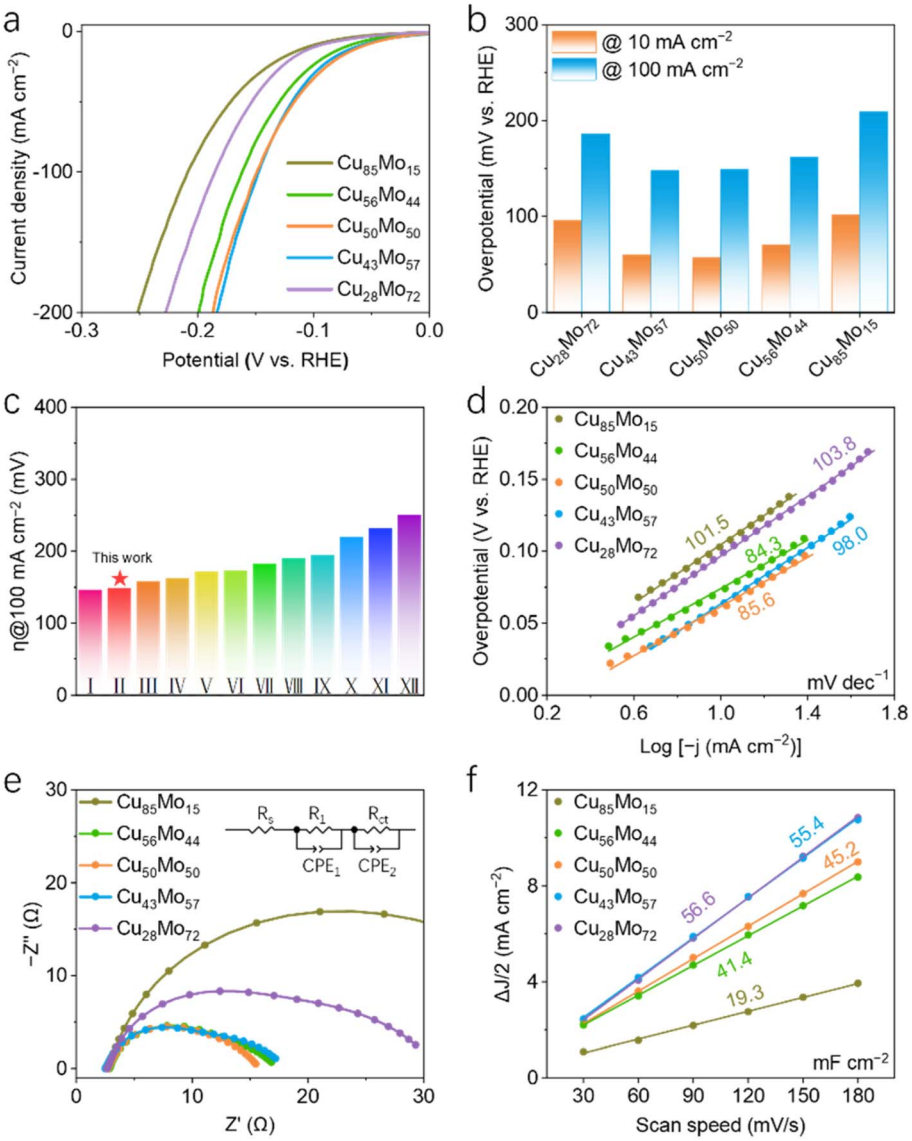

Fig. 3 HER performance of the Cu_xMo_y alloys in 1.0 M KOH. (a) LSV curves. (b) Related overpotential at 10 and 100 mA cm^{-2}. (c) Comparison of η_{100} in 1.0 M KOH with reported Mo-base or Cu-base HER catalysts. (d) Tafel plots. (e) Nyquist plots. (f) ΔJ/2 of the Cu_xMo_y alloys plotted against scan rates.

decreases, indicating that the kinetics of hydrogen evolution is gradually improved (Fig. S9b†). The charge transfer capability of the Cu_xMo_y alloys was analyzed by EIS. The Nyquist plots of the Cu_xMo_y alloys in an 0.5 M H_2SO_4 exhibit two semicircles (Fig. S9c†). The R_{ct} values of the $Cu_{43}Mo_{57}$, $Cu_{50}Mo_{50}$ and $Cu_{56}Mo_{44}$ alloys are 52.67, 49.48 and 51.61 Ω, respectively, which are smaller than those of the $Cu_{28}Mo_{72}$ (62.24 Ω) and $Cu_{85}Mo_{15}$ (62.11 Ω) alloys, implying faster charge transfer (Fig. S9c and Table S3†). The detailed fitting process of the Nyquist plot of the Cu_xMo_y alloys in 0.5 M H_2SO_4 is shown in Fig. S11.† As illustrated in Fig. S9d and S12,† the C_{dl} values of $Cu_{28}Mo_{72}$, $Cu_{43}Mo_{57}$, $Cu_{50}Mo_{50}$ and $Cu_{56}Mo_{44}$ are 64.2, 69.2, 68.1 and 62.1 mF cm^{-2}, respectively. These values indicate that the Cu_xMo_y alloys with an atomic ratio of 28 : 72 to 56 : 44 exhibit more exposed active sites in comparison to the $Cu_{85}Mo_{15}$ alloy (18.5 mF cm^{-2}).

2.3. HER durability

The stability of the Cu_xMo_y alloys was evaluated through 12 hours chronoamperometric tests (*i*–*t* tests) at a current density of 100 mA cm^{-2} in 1.0 M KOH and 0.5 M H_2SO_4. The $Cu_{28}Mo_{72}$ alloy exhibits the highest current density retention rate, and the stability of the Cu_xMo_y alloys in alkaline media is found to deteriorate as the Cu content increased (Fig. 4a). The Cu_xMo_y alloys exhibit high current density retention in an acidic medium, suggesting robust stability (Fig. S13†). Furthermore, the stability of the alloys improves gradually with an increase in the Cu content (Fig. S13†). The electrochemical test results obtained in alkaline and acidic media demonstrate that the $Cu_{50}Mo_{50}$ alloy has high catalytic activity and stability, thereby showing excellent overall performance.

HER catalysts for industrial applications require long-term stability at high current densities. Consequently, large current

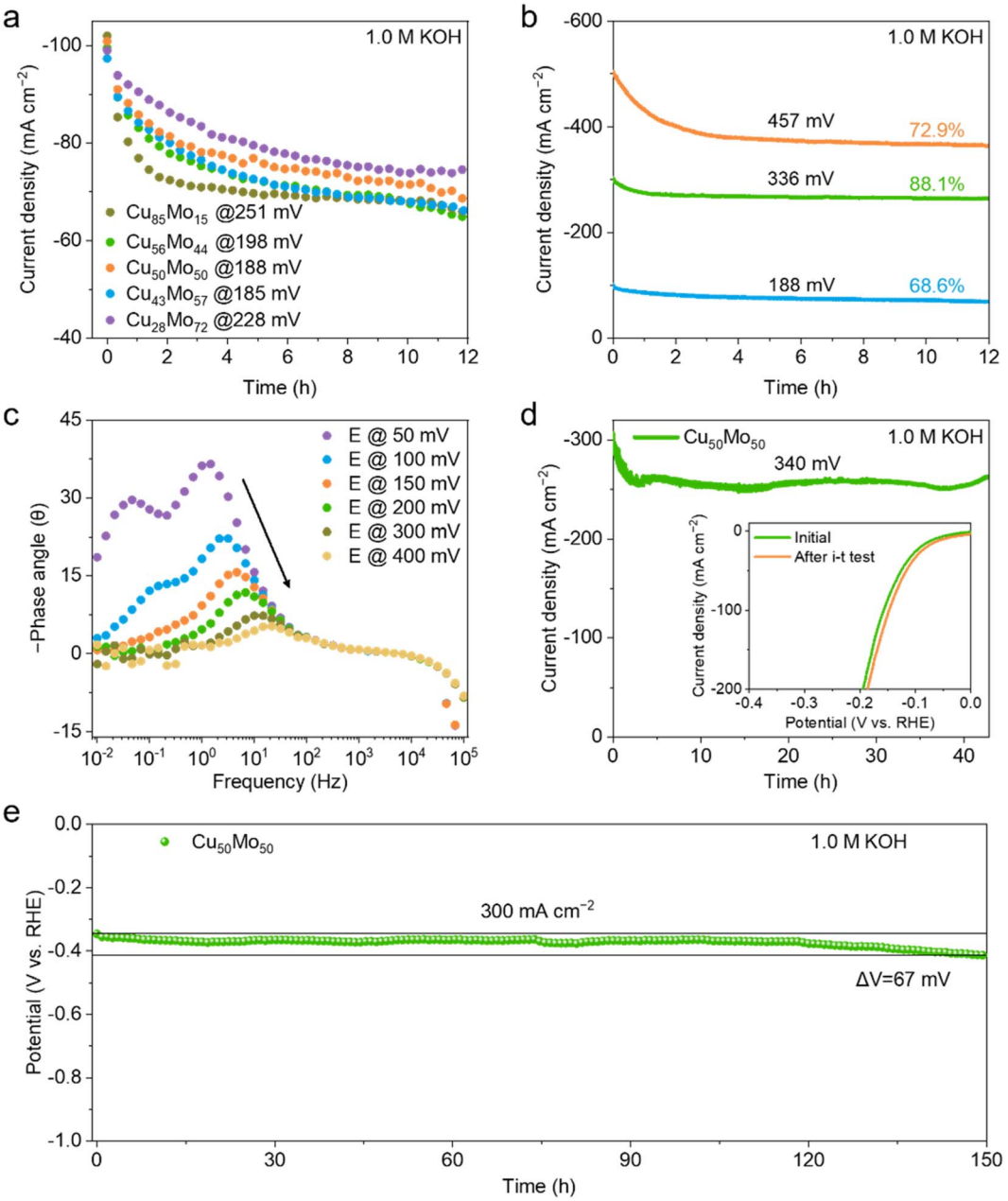

Fig. 4 (a) Chronoamperometric tests of the Cu_xMo_y alloys at 100 mA cm^{-2}. (b) Chronoamperometric tests of the $Cu_{50}Mo_{50}$ at different current densities. (c) Bode phase plots of the $Cu_{50}Mo_{50}$ alloy. (d) Long-term *i*–*t* test of the $Cu_{50}Mo_{50}$ alloy at 300 mA cm^{-2} in 1.0 M KOH. (Inset) LSV curves before and after the long-term *i*–*t* test. (e) Durability *e*–*t* test of the $Cu_{50}Mo_{50}$ alloy at 300 mA cm^{-2} in 1.0 M KOH.

density stability tests were conducted on the $Cu_{50}Mo_{50}$ alloy. As illustrated in Fig. 4b, the $Cu_{50}Mo_{50}$ alloy exhibits outstanding stability during the 300 mA cm^{-2} *i*–*t* test, with a current density retention rate of 88.1%. Furthermore, there is an almost overlapping LSV curve before and after the stability test (Fig. S14†). Following the 12 hours *i*–*t* test at 500 mA cm^{-2}, the current retention rate of the $Cu_{50}Mo_{50}$ alloy is 72.9%. In the following section, we will discuss the reasons for the deterioration of stability in the 500 mA cm^{-2} *i*–*t* test. To explore the reasons for the enhancement in the stability of the $Cu_{50}Mo_{50}$ alloy in the 300 mA cm^{-2} *i*–*t* test, an analysis of the Bode phase plots was conducted under a range of applied potentials. Fig. 4c illustrates that as the applied potential is increased, the amorphous $Cu_{50}Mo_{50}$ alloy displays an accelerated Heyrovsky step, as evidenced by the reduction in phase angle within the mid-frequency range in the Bode phase plots. The middle-frequency range (MF: 10^0–10^3 Hz) in Bode phase plots is thought to correspond to the electrochemical response of charge transfer.[38] Moreover, the phase angle within the mid-frequency range of Bode phase plots reflects the rate of Heyrovsky step.[39]

In light of the preceding analysis, we proceeded to investigate the long-term stability of the $Cu_{50}Mo_{50}$ alloy. As illustrated in Fig. 4d, a long-term *i*–*t* test at 300 mA cm^{-2} is conducted on

$Cu_{50}Mo_{50}$ in 1.0 M KOH. The current density does not exhibit a continuous attenuation during the *i–t* test, and the $Cu_{50}Mo_{50}$ alloy demonstrates a reduction in overpotential following the test (The inset in Fig. 4d). In Section 2.4, we will discuss the phenomenon of overpotential reduction after long-term *i–t* test. Furthermore, the durability of the sample is evaluated using a chronopotentiometry (*e–t*) test (Fig. 4e). The results indicate that the overpotential increases by a mere 67 mV after applying a constant current density of 300 for 150 hours. The above findings demonstrate that the amorphous $Cu_{50}Mo_{50}$ alloy exhibits remarkable high current density and long-term stability in alkaline HER process.

2.4. Characterization analysis after stability tests

To investigate the valence difference in the $Cu_{50}Mo_{50}$ alloy before and after the stability test in both alkaline and acidic media, XPS spectra of the $Cu_{50}Mo_{50}$ alloy were obtained after the 12 h *i–t* test in 1.0 M KOH and 0.5 M H_2SO_4 at 100 mA cm^{-2}. The XPS survey spectra indicates that Cu and Mo are the primary components of the $Cu_{50}Mo_{50}$ following the 12 h *i–t* test at 100 mA cm^{-2} (Fig. 5a). The high-resolution Cu 2p spectra of the $Cu_{50}Mo_{50}$ alloy after the stability test exhibits strong $Cu(OH)_2$ signals in comparison to the original $Cu_{50}Mo_{50}$ alloy (Fig. 5b). After stability test, the peaks located at 932.4–932.6 eV correspond to Cu $2p_{3/2}$ of Cu_2O (Cu^+), while the peaks located at 952.3–952.5 eV are attributed to Cu $2p_{1/2}$ of Cu_2O (Cu^+). The signals located at 934.5–934.8 and 954.3–954.5 eV are assigned to the Cu^{2+} $2p_{3/2}$ and Cu^{2+} $2p_{1/2}$, respectively. The signals observed at 941.4–946.8 and 962.3–962.6 eV are assigned to the satellite peaks of Cu^{2+}. The approximate kinetic energy positions of $Cu(OH)_2$ and Cu_2O result in only one peak being observed in the Cu LMM spectra (Fig. 5c). For the deconvoluted Mo 3d spectra of the $Cu_{50}Mo_{50}$ alloy after alkaline stability test, the peaks located at 233.88 and 236.88 eV correspond to Mo $3d_{5/2}$ and Mo $3d_{5/2}$ of Mo^{6+}, while the peaks located at 232.20 and 235.33 eV are assigned to Mo $3d_{5/2}$ and Mo $3d_{5/2}$ of Mo^{5+} (Fig. 5d). The other two peaks observed at 230.34 and 233.41 eV are attributed to Mo $3d_{5/2}$ and Mo $3d_{5/2}$ of Mo^{4+}. After the stability test in acidic condition, the $Cu_{50}Mo_{50}$ alloy exhibits a strong signal of the Mo 3d orbital, but the peak associated with Mo^{4+} is no longer visible. The XPS spectra of the O 1s of the $Cu_{50}Mo_{50}$ alloy that underwent stability tests show three discernible peaks (Fig. 5e). After stability test, the peaks located at 530.1–530.5 eV correspond to lattice oxygen, while the peaks observed at 531.3–531.7 eV are attributed to hydroxyl. The other peaks located at 533.0–533.2 eV are assigned to the adsorbed water. In 1.0 M KOH, the sample displays a stronger OH signal, whereas in 0.5 M H_2SO_4, it exhibits a stronger lattice oxygen signal ($O_{lattice}$).

The amorphous $Cu_{50}Mo_{50}$ alloy exhibits remarkable stability at 300 mA cm^{-2} in 1.0 M KOH (Fig. 4b). SEM and TEM were employed to gain insights into the morphology and composition of the amorphous $Cu_{50}Mo_{50}$ alloy after the *i–t* test at 300

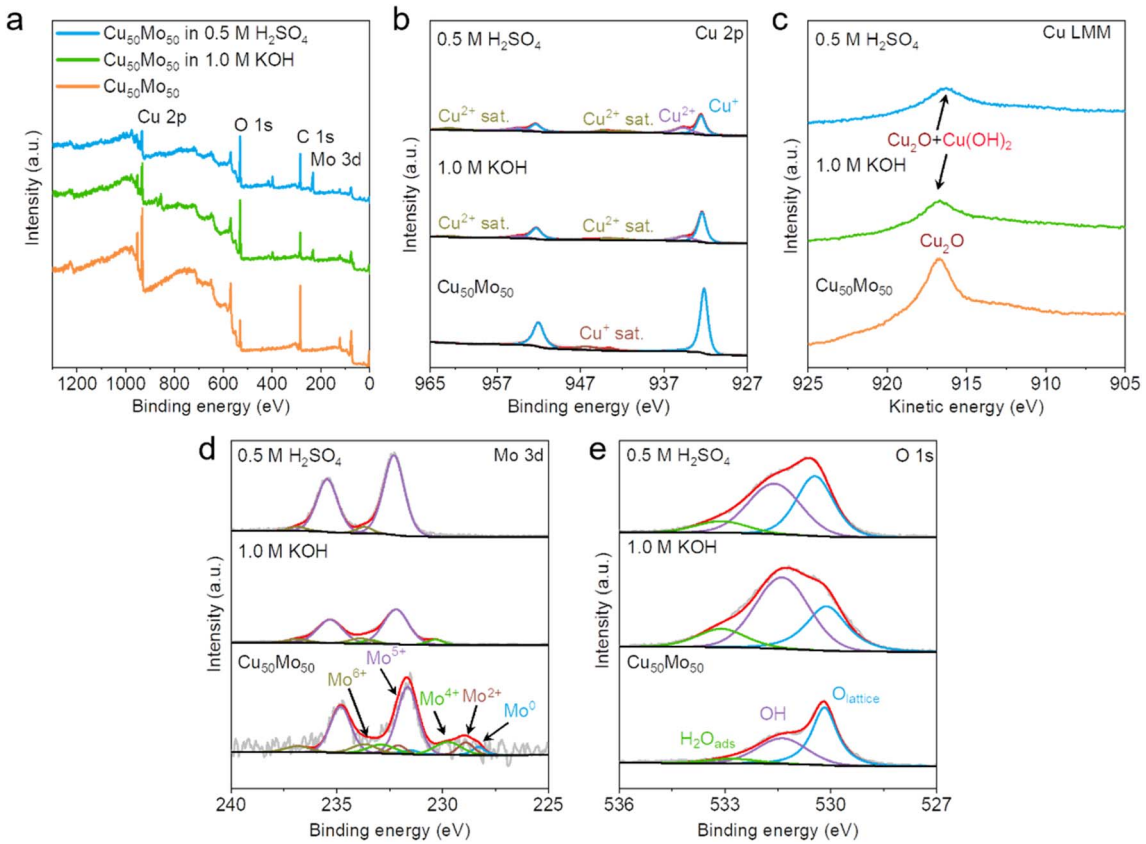

Fig. 5 XPS spectra of the $Cu_{50}Mo_{50}$ alloy after the 12 h *i–t* test at 100 mA cm^{-2}. (a) Survey spectra. (b) Cu 2p. (c) Cu LMM. (d) Mo 3d. (e) O 1s.

mA cm^{-2}. As illustrated in Fig. 6a, the surface of the $Cu_{50}Mo_{50}$ alloy exhibits sharp particles, which differ from the morphology observed in the original sample. After the stability test, the distribution of the Cu and Mo elements on the surface of the $Cu_{50}Mo_{50}$ alloy is observed to remain uniform (Fig. S15a–c†). The cross-section EDS mapping indicates that the presence of sharp particles on the surface of the sample after the stability test can be attributed to the corrosion product $Cu(OH)_2$ (Fig. S16†). As shown in Fig. 4d, after long-term *i–t* test, the sample showed an increasing chronoamperometric curve and a decreasing overpotential. This prompted us to conduct relevant characterization and tests to explore this phenomenon. The SEM images of the surface of the $Cu_{50}Mo_{50}$ alloy were obtained following *i–t* tests at 300 mA cm^{-2} over different periods (Fig. S17†). It can be found that after long-term *i–t* test, there are many holes on the surface of $Cu_{50}Mo_{50}$ alloy (Fig. S17b†), which is different from that of 12 h. The existence of holes increases the contact between catalyst and electrolyte, thus increasing active sites and improving catalytic performance. We subsequently obtained the C_{dl} prior to and following the long-term *i–t* test to assess the electrochemical active area (Fig. S18†). The C_{dl} is obtained by testing the CV at different scanning speeds in the non-Faraday region (Fig. S18b and c†). The C_{dl} values indicate that the electrochemical active area of the sample increases after long-term *i–t* test, which is consistent with the results reflected by SEM images.

Moreover, the morphologies of the $Cu_{50}Mo_{50}$ alloy were obtained after 12 hours *i–t* tests at 100 and 500 mA cm^{-2} (Fig. S19†). It can be found that under the condition of 500 mA cm^{-2}, the surface of the sample is covered with large-scale corrosion products (Fig. S19b†). The presence of this surface corrosion product hinders the contact between the catalyst and electrolyte, which deteriorates the catalytic performance. We carried out Inductively Coupled Plasma technology (ICP) tests to analyze the element content in the electrolyte after the *i–t* test (Table S4†). As shown in the ICP results, the electrolyte contains the highest amount of Mo at 300 mA cm^{-2}, and the highest amount of Cu at 500 mA cm^{-2}. When considering the stability results (Fig. 4b), it can be concluded that the factors affecting the stability of the $Cu_{50}Mo_{50}$ alloy are not only film shedding or element dissolution. It is also important to consider the impact of corrosion products on the performance of catalysts (Fig. S19†).

Fig. 6b presents a low-magnification TEM image of the $Cu_{50}Mo_{50}$ alloy after the stability test. As illustrated in Fig. 6c, the inconspicuous diffraction spots in the SAED pattern indicate that the evolution from amorphous to crystalline in the $Cu_{50}Mo_{50}$ alloy occurs during the 12 h *i–t* test at 300 mA cm^{-2}. The presence of the diffuse ring in SAED pattern shows that the amorphous structure remains in the $Cu_{50}Mo_{50}$ alloy. The amorphous structure is thermodynamically metastable, and the samples prepared by magnetron sputtering are in a non-equilibrium state. The intense hydrogen evolution reaction gradually leads to the appearance of crystalline phases in the amorphous structure. The diffraction rings are assigned to the (103) plane in MoO_3, the (113) plane in Cu_2O and the (022) plane in MoO_2 (Fig. 6c). The results in SEAD pattern demonstrate that amorphous and crystalline phases coexist in the $Cu_{50}Mo_{50}$ alloy after the stability test. The blurred lattice fringes observed in the HRTEM image and the diffused halo in the FFT pattern further

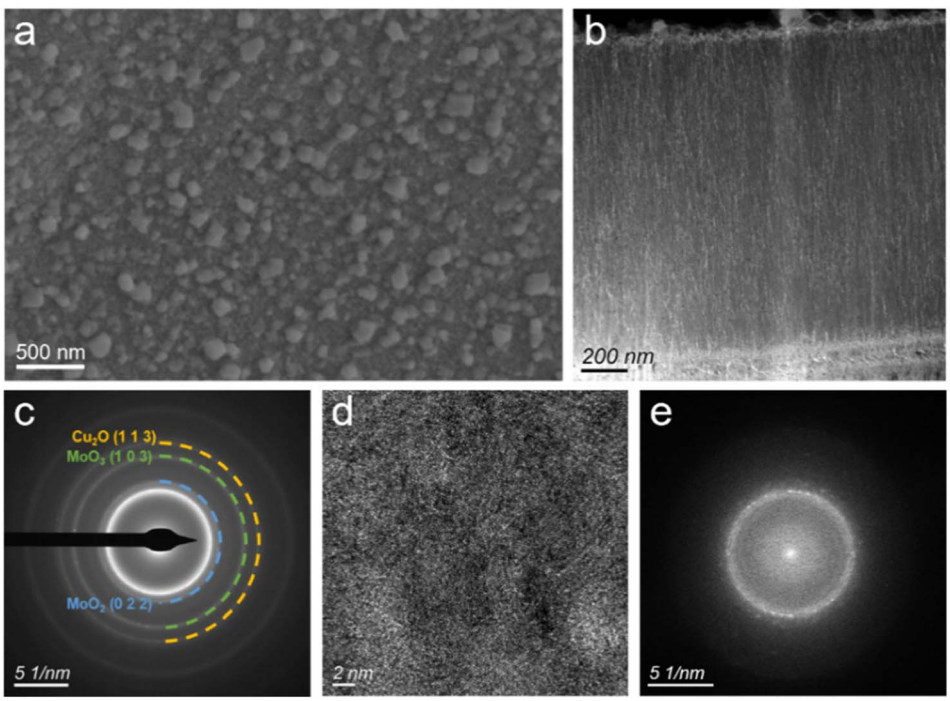

Fig. 6 SEM and TEM characterizations of the $Cu_{50}Mo_{50}$ alloy after the 12 h *i–t* test at 300 mA cm^{-2} in 1.0 M KOH. (a) SEM image. (b and c) Low-magnification TEM image and corresponding SAED pattern. (d and e) HRTEM image and corresponding FFT pattern.

illustrate the retained amorphous structure of the $Cu_{50}Mo_{50}$ alloy after the stability test (Fig. 6d and e).

2.5. HER mechanism analysis

To identify the reason for the exceptional HER performance of the Cu_xMo_y alloys, the hydrogen adsorption free energy (HBE) was evaluated through the examination of the underpotential deposited H_{upd} by means of cyclic voltammetry (CV) curves.[40] In comparison to the $Cu_{85}Mo_{15}$ alloy, the underpotentially deposited hydrogen (H_{upd}) desorption peak of the $Cu_{50}Mo_{50}$ alloy is observed to shift towards a more negative potential (Fig. 7a). This confirms the favorable hydrogen desorption step, which is attributed to the weak chemisorption strength of H. The Tafel slope results in Fig. 3d also corroborate the finding that the $Cu_{50}Mo_{50}$ alloy exhibits a more rapid Heyrovsky step (hydrogen desorption step) than the $Cu_{85}Mo_{15}$ alloy. These results demonstrate the effectiveness of alloying in improving the hydrogen adsorption strength of the Cu_xMo_y alloys.

It is important to note that the influence of OH on the catalytic reaction rate cannot be ignored in alkaline HER. Chen *et al.* verified through experiments and simulations that the adsorbed OH (OH_{ad}) plays a significant role in alkaline HER, regulating water connectivity and improving the hydrogen bonding network in the electric double layer (EDL) region.[41] Therefore, the OH adsorption capacity of the Cu_xMo_y alloys was analyzed (Fig. 7b). The $Cu_{50}Mo_{50}$ alloy demonstrate a more pronounced reversibility in the adsorption and desorption of OH compared to other Cu_xMo_y alloys. Compared with the $Cu_{85}Mo_{15}$ alloy, the smaller range of current density of the $Cu_{50}Mo_{50}$ alloy can be attributed to the rapid OH transfer process.[42] In comparison to Mo, Cu exhibits a strong OH adsorption peak, and with the Cu content increased, the OH adsorption of the Cu_xMo_y alloys displays a gradual increase (Fig. 7b).

Raman spectra were obtained for Cu and Mo at the potential of 0.85 V (V *vs.* RHE). The Raman spectrum of Cu exhibits a peak at 495 cm^{-1}, indicating a strong adsorption of OH by Cu (Fig. S20†).[43] No obvious peak was observed in the Raman spectra of Mo (Fig. S20†). Accordingly, in the alkaline HER process, Cu atoms in the Cu_xMo_y alloys work as the active sites for OH adsorption. Meanwhile, Mo atoms exhibiting high HER activity function as sites for the conversion of hydrogen. The synergistic effect of adjacent atoms significantly enhances the alkaline HER process, as isolated Cu and Mo atoms are unable to effectively promote the overall electrocatalysis process. Notably, excessive adsorption of OH will result in the poisoning

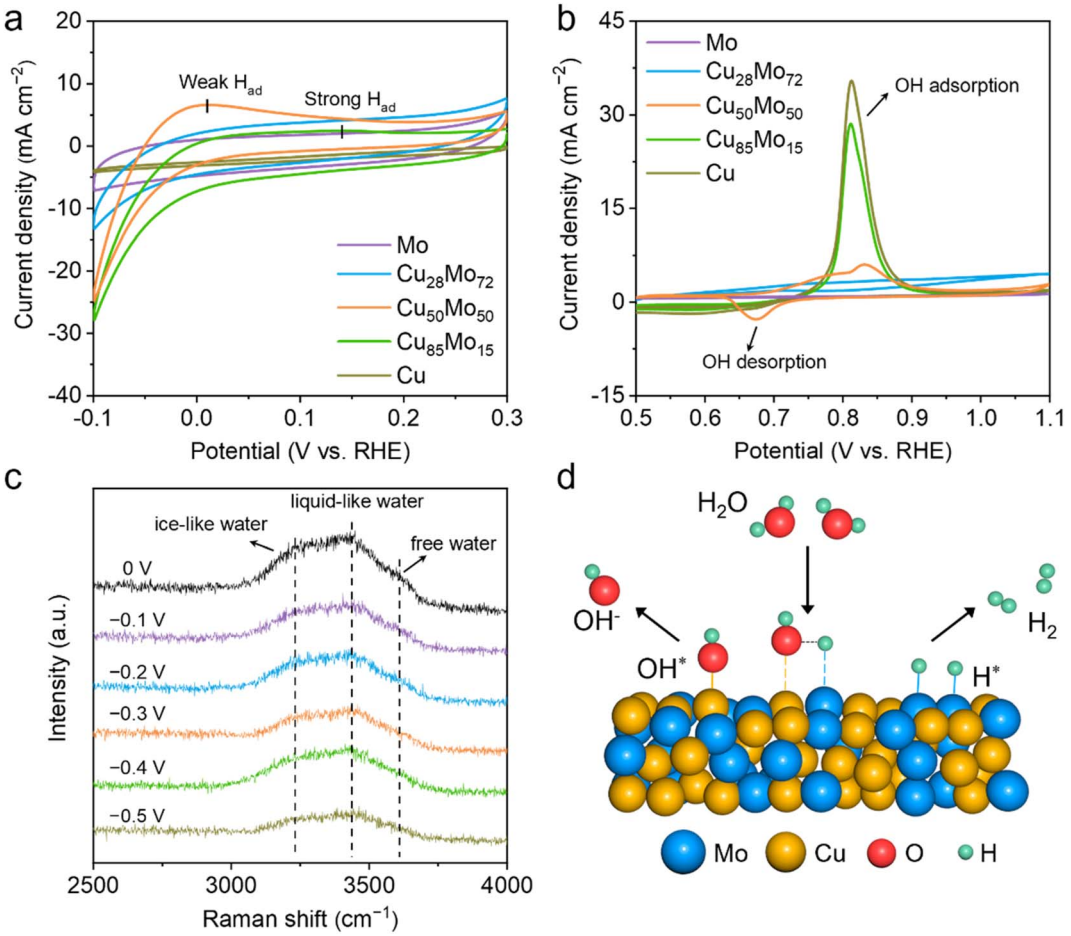

Fig. 7 (a and b) CV curves of the samples to probe hydrogen and hydroxyl adsorption features in 1.0 m KOH. (c) *In situ* Raman spectra of HER for the $Cu_{50}Mo_{50}$ alloy at different potentials. (d) Schematic representation of the alkaline HER mechanism of the amorphous $Cu_{50}Mo_{50}$ alloy.

of the active site of the catalysts, while insufficient adsorption will reduce the water dissociation ability, thus affecting the HER efficiency.[44] Therefore, the appropriate OH adsorption/desorption capacity of the catalyst is conducive to the alkaline HER process. This may be the main reason for the excellent overall alkaline HER performance of the amorphous $Cu_{50}Mo_{50}$ alloy. Due to the favorable intermediate adsorption, there is no discernible signal in the *in situ* Raman spectrum of the amorphous $Cu_{50}Mo_{50}$ alloy (Fig. S21†).

Furthermore, the interface water structure of the $Cu_{50}Mo_{50}$ alloy was investigated through *in situ* Raman spectroscopy in 1.0 M KOH (Fig. 7c). We decomposed the interfacial water peak into three peaks. The water peaks at approximately 3230 and 3440 cm^{-1} are assigned to tetrahedral (ice-like water) and trihedral ligand water (liquid-like water), respectively.[13] The peak at approximately 3610 cm^{-1} is indicative of the presence of dangling OH bonds of interfacial water, representing the free water molecules that are readily transported. The activation energies of water dissociation increased in the following sequence: the free water, the liquid-like water, and the ice-like water.[45] To gain a more intuitive understanding of the distribution of interface water, a Gaussian fitting is applied to the Raman signal of the interface water (Fig. S22†). As illustrated in Fig. S22 and S23a,† the strength of free water decreases gradually with an increase in applied potential, which proves the effective dissociation of water on the $Cu_{50}Mo_{50}$ alloy.[46] In comparison with unitary Cu and Mo, the free water strength of the $Cu_{50}Mo_{50}$ alloy demonstrates a more significant weakening within the applied potential range, thereby indicating its optimized water dissociation ability (Fig. S23†).

The synergistic effect of Mo and Cu is not only evident in the adsorption of reactants, but also in the electronic interaction between them. As an electron acceptor, Cu in the $Cu_{50}Mo_{50}$ alloy exhibits an elevated electron density, which reduces the energy barrier for the adsorption of OH (Fig. 2b). This is due to the enhanced ease with which electrons can be transferred to the O 2p orbital that adsorb OH.[47] As an electron donor, Mo in the $Cu_{50}Mo_{50}$ alloy shows more positive charge, which is thought to result in a weakened Mo–H bond (Fig. 2d).[48] The Mo–H bond energy is strong, and the reduction of electron filling to Mo–H can result in a weakening of the bond.[49] Furthermore, the enriched DOS near the Fermi level exhibited by the $Cu_{50}Mo_{50}$ alloy is thought to be conductive to the HER process (Fig. 2e).[50] The aforementioned discussion reveals the alkaline HER mechanism of the amorphous $Cu_{50}Mo_{50}$ alloy (Fig. 7d). The combination of Mo and Cu results in the effective dissociation of water molecules, with Cu acting as an adsorption site for OH and Mo acting as an adsorption site for H. Subsequently, the H* species are effectively desorbed at the Mo sites, thus producing H_2 as a result. Concurrently, the OH* species on the Cu sites transferred effectively for the subsequent reaction. This explains that the alkaline HER performance of the Cu_xMo_y alloys is more dependent on the composition than the acidic HER performance (Fig. 3a and S9a†). Furthermore, the long-range disordered structure, small grain size and high surface area of amorphous materials enhance the dual-site synergistic effect and atom utilization rate in the amorphous $Cu_{50}Mo_{50}$ alloy. Therefore, by preparing amorphous bimetallic alloys and regulating functional components, it is expected to achieve efficient water dissociation and balanced intermediate adsorption, thus promoting the alkaline HER process.

3. Conclusion

In this study, an amorphous $Cu_{50}Mo_{50}$ alloy was prepared by magnetron sputtering, which exhibited excellent hydrogen evolution reaction (HER) activity and stability. The main conclusions are as follows:

(1) The amorphous Cu_xMo_y alloys with a wide composition are prepared by magnetron sputtering for HER, a method which can be extended to the preparation of other immiscible systems catalysts for HER applications.

(2) The amorphous $Cu_{50}Mo_{50}$ catalyst exhibits a considerably low overpotential of 57 mV to reach 10 mA cm^{-2} and outstanding long-term stability at a large current density of 300 mA cm^{-2} in 1.0 M KOH. Furthermore, excellent activity with an overpotential of 120 mV at η_{10} and robust stability is observed in 0.5 M H_2SO_4 as well.

(3) Benefiting from the synergistic effect of dual active sites, the amorphous $Cu_{50}Mo_{50}$ alloy with modified electronic structure shows optimized water dissociation and good intermediate adsorption capacity, thus accelerating the alkaline HER process.

This work offers a viable approach for the preparation of immiscible alloys with high HER activity, while also providing valuable insights for the design of efficient alkaline HER catalysts.

Data availability

The data that support the findings of this study are available on request from the corresponding authors upon reasonable request.

Conflicts of interest

There are no conflicts to declare.

Acknowledgements

This work was financially supported by Guangdong Basic and Applied Basic Research Foundation (No. 2024B1515020010), Guangzhou Science and Technology Plan Project (No. 2025A04J4432) and the Fundamental Research Funds for the Central Universities (No. 21623103).

References

1 Y. Pan, J. Gao, E. Lv, T. Li, H. Xu, L. Sun, A. Nairan and Q. Zhang, *Adv. Funct. Mater.*, 2023, **33**, 2303833.
2 M. Liu, Z. Yao, J. Gu, C. Li, X. Huang, L. Zhang, Z. Huang and M. Fan, *Chem. Eng. J.*, 2023, **461**, 141918.
3 Y. Li, X. Wei, L. Chen and J. Shi, *Angew. Chem., Int. Ed.*, 2021, **60**, 19550–19571.

4 W. Du, Y. Shi, W. Zhou, Y. Yu and B. Zhang, *Angew. Chem., Int. Ed.*, 2021, **60**, 7051–7055.
5 X. Wang, Q. Peng, X. Zhang, X. Lv, X. Wang and Y. Fu, *J. Colloid Interface Sci.*, 2022, **607**, 1580–1588.
6 T. Xiong, J. Li, J. Chandra Roy, M. Koroma, Z. Zhu, H. Yang, L. Zhang, T. Ouyang, M. S. Balogun and M. Al-Mamun, *J. Energy Chem.*, 2023, **81**, 71–81.
7 G. Zhong, R. Zhao, Y.-R. Shi, C.-R. Li, L. He, L. He and Y. Huang, *Rare Met.*, 2023, **42**, 2166–2173.
8 Z. Wu, P. Yang, Q. Li, W. Xiao, Z. Li, G. Xu, F. Liu, B. Jia, T. Ma, S. Feng and L. Wang, *Angew. Chem.*, 2023, **135**, e202300406.
9 Y. Zhu, M. Klingenhof, C. Gao, T. Koketsu, G. Weiser, Y. Pi, S. Liu, L. Sui, J. Hou, J. Li, H. Jiang, L. Xu, W.-H. Huang, C.-W. Pao, M. Yang, Z. Hu, P. Strasser and J. Ma, *Nat. Commun.*, 2024, **15**, 1447.
10 S. M. El-Refaei, P. A. Russo, T. Schultz, Z. N. Chen, P. Amsalem, N. Koch and N. Pinna, *Carbon Energy*, 2024, **6**, e556.
11 Y. Kuang, W. Qiao, F. Yang and L. Feng, *J. Energy Chem.*, 2023, **85**, 447–454.
12 Y. Zhang, H. Guo, X. Li, J. Du, W. Ren and R. Song, *Chem. Eng. J.*, 2021, **404**, 126483.
13 P. Yang, F. Liu, X. Zang, L. Xin, W. Xiao, G. Xu, H. Li, Z. Li, T. Ma, J. Wang, Z. Wu and L. Wang, *Adv. Energy Mater.*, 2024, **14**, 2303384.
14 S. Hussain, I. Rabani, D. Vikraman, A. Feroze, M. Ali, Y.-S. Seo, W. Song, K.-S. An, H.-S. Kim, S.-H. Chun and J. Jung, *Chem. Eng. J.*, 2021, **421**, 127843.
15 D. Zhao, K. Sun, W. C. Cheong, L. Zheng, C. Zhang, S. Liu, X. Cao, K. Wu, Y. Pan, Z. Zhuang, B. Hu, D. Wang, Q. Peng, C. Chen and Y. Li, *Angew. Chem.*, 2020, **132**, 9067–9075.
16 Z. Zhao, J. Sun, X. Li, S. Qin, C. Li, Z. Zhang, Z. Li and X. Meng, *Nat. Commun.*, 2024, **15**, 7475.
17 J. Wang, Y. Gao, H. Kong, J. Kim, S. Choi, F. Ciucci, Y. Hao, S. Yang, Z. Shao and J. Lim, *Chem. Soc. Rev.*, 2020, **49**, 9154–9196.
18 M. M. Jakšić, *Int. J. Hydrogen Energy*, 1987, **12**, 727–752.
19 Q. Cao, Y. Yuan, K. Wang, W. Huang, Y. Zhao, X. Sun, R. Ding, W. Lin, E. Liu and P. Gao, *J. Colloid Interface Sci.*, 2022, **618**, 411–418.
20 M. P. Marčeta Kaninski, D. L. Stojić, Đ. P. Šaponjić, N. I. Potkonjak and Š. S. Miljanić, *J. Power Sources*, 2006, **157**, 758–764.
21 M. B. Gawande, A. Goswami, F.-X. Felpin, T. Asefa, X. Huang, R. Silva, X. Zou, R. Zboril and R. S. Varma, *Chem. Rev.*, 2016, **116**, 3722–3811.
22 J. Wang, B. Guo, J. Sun, Y. Zhou, C. Zhao, Z. Wei and J. Guo, *Appl. Catal., B*, 2023, **324**, 122169.
23 J.-X. Feng, J.-Q. Wu, Y.-X. Tong and G.-R. Li, *J. Am. Chem. Soc.*, 2018, **140**, 610–617.
24 L. Peng, D. Zhang, Z. Ma, D. Chu, C. Cazorla, R. Amal and Z. Han, *Small Struct.*, 2023, **4**, 2300194.
25 Z. Tao, H. Zhao, N. Lv, X. Luo, J. Yu, X. Tan and S. Mu, *Adv. Funct. Mater.*, 2024, **34**, 2312987.
26 Y. Zhang, F. Gao, D. Wang, Z. Li, X. Wang, C. Wang, K. Zhang and Y. Du, *Coord. Chem. Rev.*, 2023, **475**, 214916.
27 S. Anantharaj and S. Noda, *Small*, 2020, **16**, 1905779.
28 T. Guo, L. Li and Z. Wang, *Adv. Energy Mater.*, 2022, **12**, 2200827.
29 M. Luo, W. Peng, Y. Zhao, J. Lan, M. Peng, J. Han, H. Li and Y. Tan, *Scr. Mater.*, 2021, **191**, 56–61.
30 H. Kim, E. Hwang, H. Park, B.-S. Lee, J. H. Jang, H.-J. Kim, S. H. Ahn and S.-K. Kim, *Appl. Catal., B*, 2017, **206**, 608–616.
31 M. Sun, Q. Ye, L. Lin, Y. Wang, Z. Zheng, F. Chen and Y. Cheng, *J. Colloid Interface Sci.*, 2023, **637**, 262–270.
32 D. Zhang, H. Li, A. Riaz, A. Sharma, W. Liang, Y. Wang, H. Chen, K. Vora, D. Yan, Z. Su, A. Tricoli, C. Zhao, F. J. Beck, K. Reuter, K. Catchpole and S. Karuturi, *Energy Environ. Sci.*, 2022, **15**, 185–195.
33 X. Jian, W. Zhang, Y. Yang, Z. Li, H. Pan, Q. Gao and H.-J. Lin, *ACS Catal.*, 2024, **14**, 2816–2827.
34 T. Liu, W. Gao, Q. Wang, M. Dou, Z. Zhang and F. Wang, *Angew. Chem., Int. Ed.*, 2020, **59**, 20423–20427.
35 Y. Yan, T. Meng, Y. Chen, Y. Yang, D. Wang, Z. Xing and X. Yang, *J. Energy Chem.*, 2024, **88**, 356–362.
36 Z. Zhang, L. Li, Y. Li, Y. Zheng, Q. Wu, L. Xie, B. Luo, J. Hao and W. Shi, *Chem. Eng. J.*, 2023, **469**, 143846.
37 Y. Oh, J. Theerthagiri, A. Min, C. J. Moon, Y. Yu and M. Y. Choi, *Carbon Energy*, 2024, **6**, e448.
38 Y. Qiu, X. Tu, X. Lu and J. Yang, *Corros. Sci.*, 2022, **199**, 110177.
39 Y. Zhang, J. Lan, Y. Xu, Y. Yan, W. Liu, X. Liu, S. Gu, J. Zhou and M. Wang, *J. Colloid Interface Sci.*, 2024, **660**, 997–1009.
40 Y. Guo, W. He, X. Tan, Y. Xiao, B. Du, C. Wang, H. Cui, Y. Li and C. Wang, *Adv. Funct. Mater.*, 2025, **35**, 2412142.
41 P. Li, Y. Jiang, Y. Hu, Y. Men, Y. Liu, W. Cai and S. Chen, *Nat. Catal.*, 2022, **5**, 900–911.
42 X. Wang, G. Long, B. Liu, Z. Li, W. Gao, P. Zhang, H. Zhang, X. Zhou, R. Duan, W. Hu and C. Li, *Angew. Chem., Int. Ed.*, 2023, **62**, e202301562.
43 L. Xiao, W. Dai, S. Mou, X. Wang, Q. Cheng and F. Dong, *Energy Environ. Sci.*, 2023, **16**, 2696–2704.
44 H. Ren, Z. Zhang, Z. Geng, Z. Wang, F. Shen, X. Liang, Z. Cai, Y. Wang, D. Cheng, Y. Cao, X. Yang, M. Hu, X. Yao and K. Zhou, *Adv. Energy Mater.*, 2024, 2400777.
45 X. H. Chen, X. L. Li, T. Li, J. H. Jia, J. L. Lei, N. B. Li and H. Q. Luo, *Energy Environ. Sci.*, 2024, **17**, 5091–5101.
46 Z. Wu, Q. Li, G. Xu, W. Jin, W. Xiao, Z. Li, T. Ma, S. Feng and L. Wang, *Adv. Mater.*, 2024, **36**, 2311018.
47 X. B. Zhang, L. Xia, G. Zhao, B. Zhang, Y. Chen, J. Chen, M. Gao, Y. Jiang, Y. Liu, H. Pan and W. Sun, *Adv. Mater.*, 2023, **35**, 2208821.
48 B. Ren, D. Li, Q. Jin, H. Cui and C. Wang, *J. Mater. Chem. A*, 2017, **5**, 24453–24461.
49 Y. Ma, M. Chen, H. Geng, H. Dong, P. Wu, X. Li, G. Guan and T. Wang, *Adv. Funct. Mater.*, 2020, **30**, 2000561.
50 J. Zhang, Y. Gu, Y. Lu, C. Zhu, G. Liu, C. Wang, D. Sun, Y. Tang and H. Sun, *Appl. Catal., B*, 2023, **325**, 122316.